Seasonal Variation of the South Equatorial Current Bifurcation off Madagascar

ZHAOHUI CHEN AND LIXIN WU

Physical Oceanography Laboratory/Qingdao Collaborative Innovation Center of Marine Science and Technology, Ocean University of China, Qingdao, China

BO QIU

Department of Oceanography, University of Hawai'i at Mānoa, Honolulu, Hawaii

SHANTONG SUN AND FAN JIA

Physical Oceanography Laboratory/Qingdao Collaborative Innovation Center of Marine Science and Technology, Ocean University of China, Qingdao, China

(Manuscript received 26 June 2013, in final form 26 October 2013)

ABSTRACT

In this paper, seasonal variation of the South Equatorial Current (SEC) bifurcation off the Madagascar coast in the upper south Indian Ocean (SIO) is investigated based on a new climatology derived from the World Ocean Database and 19-year satellite altimeter observations. The mean bifurcation integrated over the upper thermocline is around 18°S and reaches the southernmost position in June/July and the northernmost position in November/December, with a north–south amplitude of about 1°. It is demonstrated that the linear, reduced gravity, long Rossby model, which works well for the North Equatorial Current (NEC) bifurcation in the North Pacific, is insufficient to reproduce the seasonal cycle and the mean position of the SEC bifurcation off the Madagascar coast. This suggests the importance of Madagascar in regulating the SEC bifurcation. Application of Godfrey's island rule reveals that compared to the zero Sverdrup transport latitude, the mean SEC bifurcation is shifted poleward by over 0.8° because of the meridional transport of about 5 Sverdrups (Sv; $1\,\mathrm{Sv} \equiv 10^6\,\mathrm{m^3\,s^{-1}}$) between Madagascar and Australia. A time-dependent linear model that extends the Godfrey's island rule is adopted to examine the seasonal variation of the SEC bifurcation. This time-dependent island rule model simulates the seasonal SEC bifurcation well both in terms of its mean position and peak seasons. It provides a dynamic framework to clarify the baroclinic adjustment processes involved in the presence of an island.

1. Introduction

Under the southeasterly trade winds, the South Equatorial Current (SEC) in the south Indian Ocean (SIO) flows westward between 8° and 20°S. Upon encountering the eastern Madagascar coast, the SEC bifurcates into the North Madagascar Current (NMC) and the East Madagascar Current (EMC), both of which are believed to play a crucial role in redistributing mass and heat along the Madagascar coast and farther to the downstream current systems (e.g., Lutjeharms et al. 1981; Swallow et al. 1988; Schott et al. 1988; Hastenrath and Greischar 1991; Stramma and Lutjeharms 1997; Schott and McCreary 2001; Matano et al. 2002; Donohue and Toole 2003; Palastanga et al. 2006, 2007; Nauw et al. 2008; Siedler et al. 2009; Ridderinkhof et al. 2010). Previous studies have mainly focused on the position of the SEC bifurcation off the Madagascar coast in the near-surface layer (around 17°S) or at the intermediate depths (20°S) (e.g., Swallow et al. 1988; Chapman et al. 2003). The vertical structure of the SEC bifurcation, on the other hand, has received less attention due to the lack of comprehensive observational data in this region. Meanwhile, the large-scale ocean circulation in the SIO exhibits distinct seasonal variation due to the strong monsoonal wind forcing [see Schott and McCreary (2001) for a comprehensive review] and our knowledge about the seasonal SEC bifurcation off the Madagascar coast remains incomplete.

Corresponding author address: Zhaohui Chen, Physical Oceanography Laboratory, Ocean University of China, 5 Yushan Road, Qingdao, 266003, China.
E-mail: chenzhaohui@ouc.edu.cn

DOI: 10.1175/JPO-D-13-0147.1

In the Pacific Ocean, the bifurcation of the North Equatorial Current (NEC) off the Philippine coast has been intensively studied over the past two decades. The multi–time scale variability has been investigated both observationally (Toole et al. 1990; Qu and Lukas 2003; Wang and Hu 2006; Qiu and Chen 2010) and numerically (Qiu and Lukas 1996; Kim et al. 2004; Jensen 2011; Chen and Wu 2011, 2012). These studies have systematically explored the NEC bifurcation and have improved our understanding of the low-latitude western boundary current dynamics. However, to our knowledge, no attempt has been made to describe and understand the variability of the SEC bifurcation in the SIO.

It has been shown in previous studies that the equatorial current bifurcation off the western boundary is the most prominent phenomena in the upper-layer ocean, and the baroclinic adjustment (i.e., interplay between local wind forcing and remote baroclinic Rossby wave propagation) is responsible for its seasonal variation in the North Pacific Ocean (Qiu and Lukas 1996; Chen and Wu 2011, 2012) and the South Atlantic Ocean (e.g., Rodrigues et al. 2007). The presence of Madagascar Island, however, makes the western boundary topography in the SIO different from that in the Pacific/Atlantic. The Godfrey (1989) island rule shows that a planetary-scale island can significantly alter the western boundary current structure, and it is speculated that the existence of Madagascar could affect the SEC bifurcation because its meridional extent spans almost 1500 km (the northern and southern tips of Madagascar are at 12° and 25°S, respectively). The objective of the present study is to elucidate the role of Madagascar in determining the mean and seasonal variation of the SEC bifurcation latitude.

This paper is organized as follows: Section 2 gives a brief description of the data and methods, followed by a general description of the mean SEC bifurcation as well as its seasonal cycle. In section 3, the role of Madagascar Island in governing the SEC bifurcation is discussed. The summary and discussion are presented in section 4.

2. Data and methods

a. World Ocean Database

High-resolution conductivity–temperature–depth (CTD) data, low-resolution CTD, expendable CTD (XCTD), Ocean Station Data (OSD), expendable bathythermograph data (XBT), profiling float data (PFL), and moored buoy data (MRB) at observed levels from an updated version of the *World Ocean Database 2009* (*WOD09*) of the National Oceanographic Data Center (NODC; Boyer et al. 2009) are used to construct the monthly climatological temperature and salinity fields in the region of 30°–10°S, 40°–70°E. Following Qu and Lukas (2003), we first choose the available data through quality control: profiles with apparent erroneous records (e.g., temperature lower than 5°C at the surface) and data that are 3 times greater than the standard deviation at respective levels are excluded.

The geographic distributions of the available temperature–salinity profiles are shown in Figs. 1a and 1b. There are 42 766 profiles of temperature and 20 581 profiles of salinity in the selected region after quality control. The profiles are not uniformly scattered, most are distributed around Mauritius and along repeated hydrographic sections. The number of temperature–salinity profiles in the bifurcation area is somewhat sparse (generally less than 100 temperature profiles and 50 salinity profiles in the selected box), but is sufficient for our study because we focus on the seasonal variation. Vertical distributions of the available profiles are confined mainly to the upper 400 m, and only a quarter of them extend deeper than 1000 m (Fig. 1c). Because we are interested in the upper-layer bifurcation signals, the sparse data distribution in the deep ocean does not impose too serious a problem to the present study. Figure 1d shows the histogram of the temperature–salinity profiles as a function of months, and to a large degree they are uniformly distributed without seasonal biases.

The temperature–salinity data from individual profiles are first interpolated onto a vertical grid of 10-m intervals between the surface and 1500 m using cubic spline. After that, the data are mapped onto a $0.5° \times 0.5°$ grid at each level using an objective mapping technique following Qiu et al. (2013). The gridded monthly data are then smoothed horizontally using a two-dimensional Gaussian filter with an e-folding scale of 1.5° to reduce the noise produced by eddies, internal waves, and tides. Finally, the temperature–salinity fields are converted to dynamic heights with the reference level at 1500 dbar, and the geostrophic velocities are derived subsequently.

The depth-integrated (0–400 m) dynamic height and flow are shown in Fig. 2a, which provides a general picture of the upper-layer geostrophic circulation in the SIO. The SEC, as depicted in Fig. 2b, is most prominent in the upper 400 m and exhibits a poleward tilting with increasing depth that is consistent with the zonal flow structures in the Pacific and Atlantic Oceans (e.g., Qu and Lindstrom 2002; Qu and Lukas 2003; Rodrigues et al. 2007). In addition, the subtropical South Indian Ocean Countercurrent (SICC) is captured at around 25°S in the upper 250 m, which is in agreement with recent observational studies (Siedler et al. 2006; Palastanga et al. 2007; Jia et al. 2011). The SEC bifurcation structure derived from the geostrophic velocity is shown in Fig. 2c. Here the bifurcation latitude is defined at where the meridional velocity averaged within a 2°-longitude

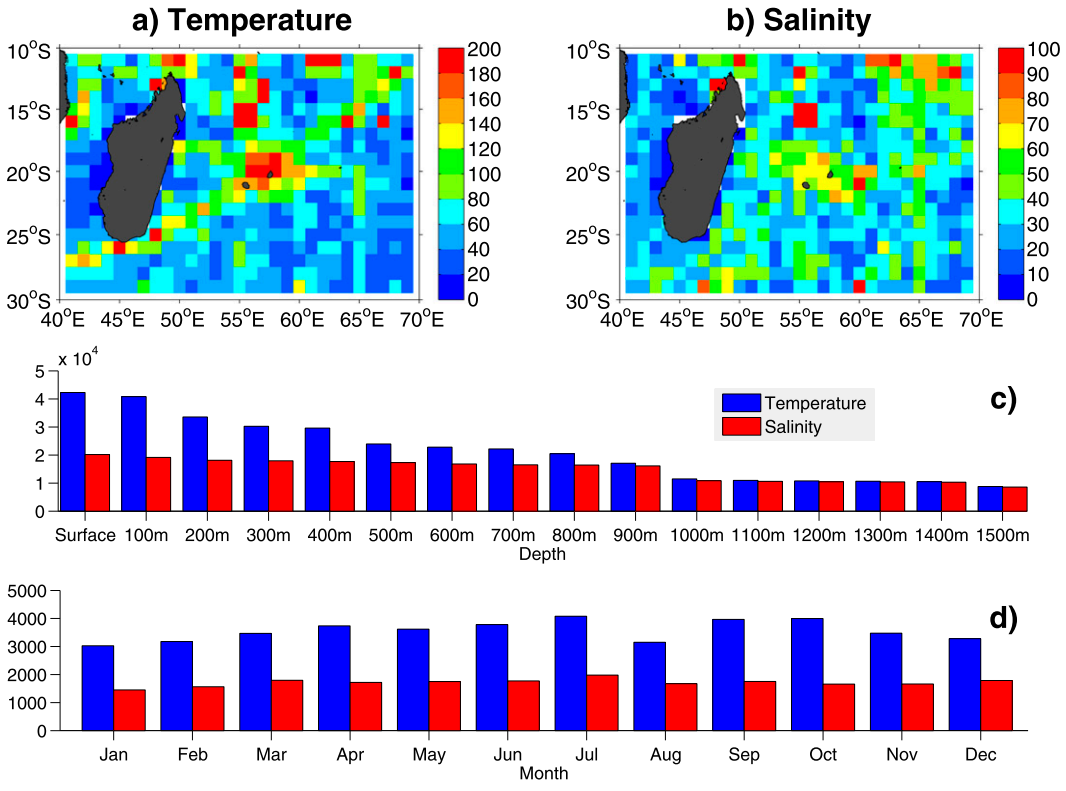

FIG. 1. Number of (a) temperature and (b) salinity profiles in 1° × 1° boxes of the southwest Indian Ocean from the *WOD09*. (c) Histogram of the temperature–salinity profiles observed in each level. (d) Histogram of the temperature–salinity profiles as a function of months.

band off the coast is zero because the typical width of the western boundary current along the Madagascar coast is over 150 km (Swallow et al. 1988; Schott et al. 1988; Donohue and Toole 2003; Nauw et al. 2008). Figure 2c reveals that the SEC bifurcation latitude (SBL) shifts from 17.5°S at the surface to 19°S at 400 m, with its depth mean position at 18.1°S. If the surface Ekman drift driven by the local winds is considered, the mean SBL moves slightly northward to 17.9°S.

b. *Satellite altimetry sea surface height data*

Satellite altimetry provides a global, high-resolution, and all-weather description of the sea level variation, which mainly reflects the surface-layer ocean circulation. In this study, we use the global sea surface height (SSH) anomaly dataset that merges the Ocean Topography Experiment (TOPEX)/Poseidon, *European Remote Sensing Satellite 1* and *2* (*ERS-1* and *ERS-2*),

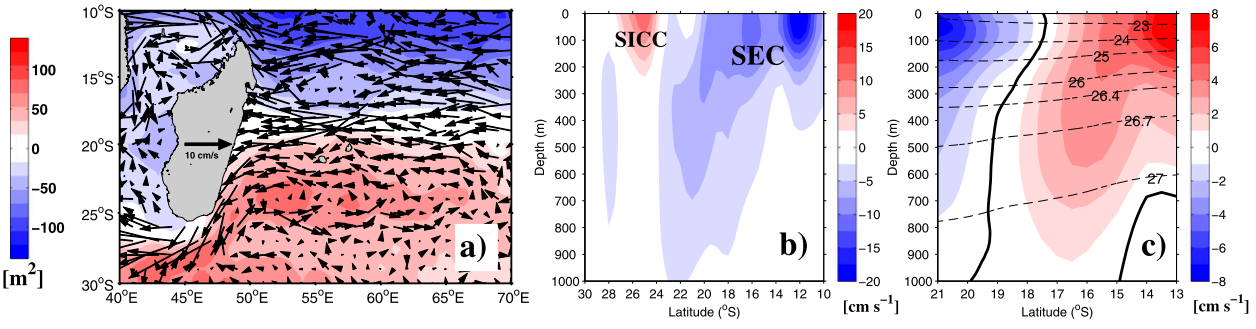

FIG. 2. (a) Mean depth-integrated (0–400 m) dynamic height and geostrophic flow relative to 1500 dbar. The area-mean value is removed. (b) Zonal geostrophic velocity at 52°E. (c) Meridional geostrophic velocity averaged within a 2°-lon band off the Madagascar coast (shaded). The boldface line indicates the SEC bifurcation and the dashed contours are the potential density σ_θ calculated from the temperature–salinity data.

Geosat Follow-On, and *Jason-1* and *Jason-2* along-track SSH measurements. The dataset has a weekly format on a ⅓° × ⅓° Mercator grid and covers the period from October 1992 to December 2011. The weekly dataset is temporally averaged to form the monthly SSH anomaly dataset in this study.

The climatological SSH field is required for determining the bifurcation of the SEC. We adopt the hybrid mean dynamic topography by Rio et al. (2011) that combines the Gravity Recovery and Climate Experiment (GRACE) geoid, surface-drifter velocities, profiling float, and hydrographic temperature–salinity data. Following Qiu and Chen (2010), the monthly meridional geostrophic velocity v_g is calculated as a function of y along the Madagascar coast:

$$v_g(y,t) = \frac{g}{fL}[\mathrm{ssh}_E(y,t) - \mathrm{ssh}_W(y,t)], \qquad (1)$$

where g is the gravitational acceleration, f is the Coriolis parameter, ssh_W is the absolute SSH value (mean dynamic topography plus SSH anomaly) averaged within the 1° band east of the Madagascar coast, ssh_E is the absolute SSH value averaged within the 1° band farther eastward, and L is the distance between the points E and W. SBL at the surface is determined by the location where $v_g = 0$. For multiple zero v_g along the Madagascar coast, we follow Qiu and Chen (2010) and set the SEC bifurcation at the latitude where we can trace the SSH contour at the $v_g = 0$ point back to the core of the westward-flowing SEC.

c. *Seasonal variation of the SEC bifurcation off the Madagascar coast*

In addition to the above-mentioned two datasets, a newly developed operational ocean reanalysis system 4 (ORA-S4) of the European Centre for Medium-Range Weather Forecasts (ECMWF) (Balmaseda et al. 2012) is also used to examine the seasonal cycle of SBL. The mean SBL integrated over the upper 400 m is located at 18.1°S based on the calculations from both the *WOD09* and the ECMWF ORA-S4, but is located at 16.9°S from the 19-year altimetry SSH data analysis (Fig. 3). This 1.2° difference is largely due to the poleward tilting of the SEC bifurcation with increasing depth (Fig. 2c). In terms of its seasonal variation, SBL moves to the southernmost position in June/July and the northernmost position in November/December, with its amplitude of about 0.8°–1° in the upper 400-m layer and 1.5° at the surface.

The seasonal north–south migration of the SEC bifurcation in the SIO is analogous to that in the North Pacific and the South Atlantic, implying bifurcations of the equatorial currents in the upper thermocline share

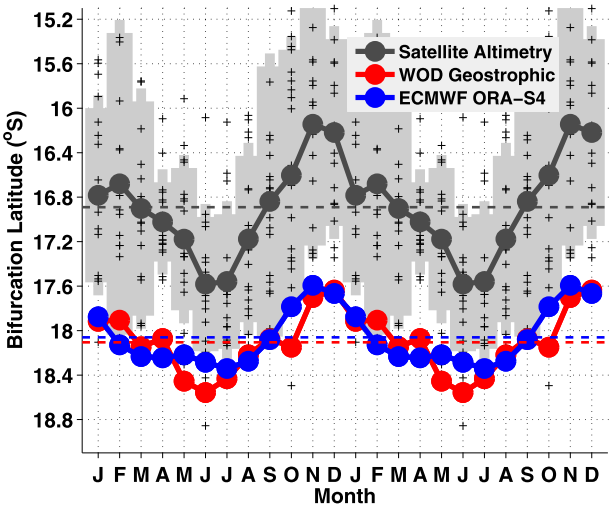

FIG. 3. Seasonal variation of the SEC bifurcation lat derived from the satellite altimetry SSH data (black), the geostrophic flow averaged in the upper 400 m (red), and the meridional flow averaged in the upper 415 m from the new ECMWF ORA-S4 product (blue). The pluses denote individual bifurcation lat estimated from the SSH data and the shaded bars denote the std dev range. The dashed lines are mean values.

the same governing dynamics (e.g., Qiu and Lukas 1996; Kim et al. 2004; Rodrigues et al. 2007; Chen and Wu 2011, 2012). In the North Pacific, for example, baroclinic adjustment processes have been highlighted to play a leading role in governing the seasonal variation of the NEC bifurcation. In the next section, a series of numerical experiments and analytical analyses will be conducted in order to clarify the dynamics that control the seasonal bifurcation of the SEC in the SIO.

3. Dynamics of the SEC bifurcation off Madagascar: Mean position and seasonal variation

a. *Wind stress pattern over the Indian Ocean*

It is instructive to first examine the wind stress pattern over the Indian Ocean. The wind stress data analyzed in this study are derived from the ECMWF ORA system 3 (ORA-S3), which is believed to be one of the most reliable ocean reanalysis products (Balmaseda et al. 2008). Figure 4a shows that the wind stress over the SIO is characterized by the southeasterly trade winds with the wind stress curl pattern being approximately zonal. The mean position of the zero zonally integrated wind stress curl line is along 17.45°S. The seasonal amplitude of the zero wind stress curl line, shown in Fig. 4c, is almost 8 times larger than that of the SBL. Meanwhile, the peak season of wind forcing leads the SBL by 2–4 months, similar to those in the North Pacific (Qu and Lukas 2003).

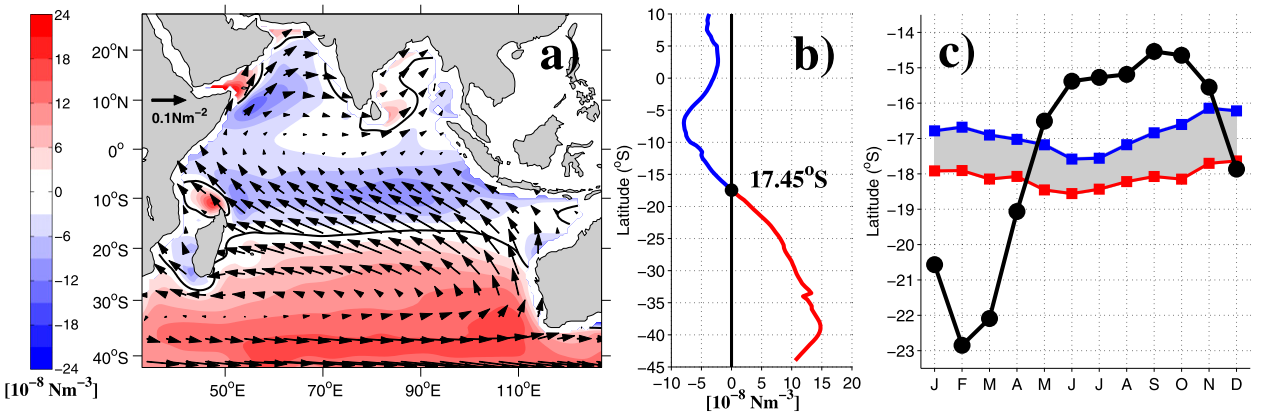

FIG. 4. (a) Mean wind stress and wind stress curl derived from ECMWF ORA-S3. The solid lines indicate the zero contours. (b) Mean value of the zonally integrated wind stress curl as a function of lat. (c) Seasonal evolution of the lat of the zero wind stress curl line in the SIO (black), observed SBL at the surface (blue) from the altimetry SSH data, and upper 400-m mean (red) from *WOD09*.

b. *Modeling the seasonal cycle of SBL with the linear, reduced gravity, long Rossby model*

It has been shown that the seasonal cycle of the NEC bifurcation in the North Pacific is well reproduced by the linear, reduced gravity, long Rossby model [hereinafter the Rossby model; see Fig. 9 in Chen and Wu (2012)]. We first use this model to simulate the SBL in the SIO. To evaluate its performance in simulating the seasonal variation of the SEC bifurcation off the Madagascar coast, several parallel experiments are set up using both the Rossby model and the 1.5-layer nonlinear reduced gravity model (denoted below as the 1.5-layer model for brevity). The detailed governing equations as well as the configurations for these two models are given in the appendix. All model runs are forced by the monthly climatological wind stress curl/wind stresses of ORA-S3.

It is demonstrated in Fig. 5a that the observed seasonal cycle of the NEC bifurcation off the Philippines is well reproduced in both the Rossby model and the 1.5-layer model. This confirms that the relevant dynamics mentioned above are capable of describing the seasonal variation. Likewise, the SEC bifurcation off the Madagascar coast simulated in the 1.5-layer model roughly coincides with the observed seasonal cycle in terms of the mean position, seasonal north–south migration, and peak seasons (Fig. 5b). This indicates that the 1.5-layer model, in which only the baroclinic processes are involved, is capable

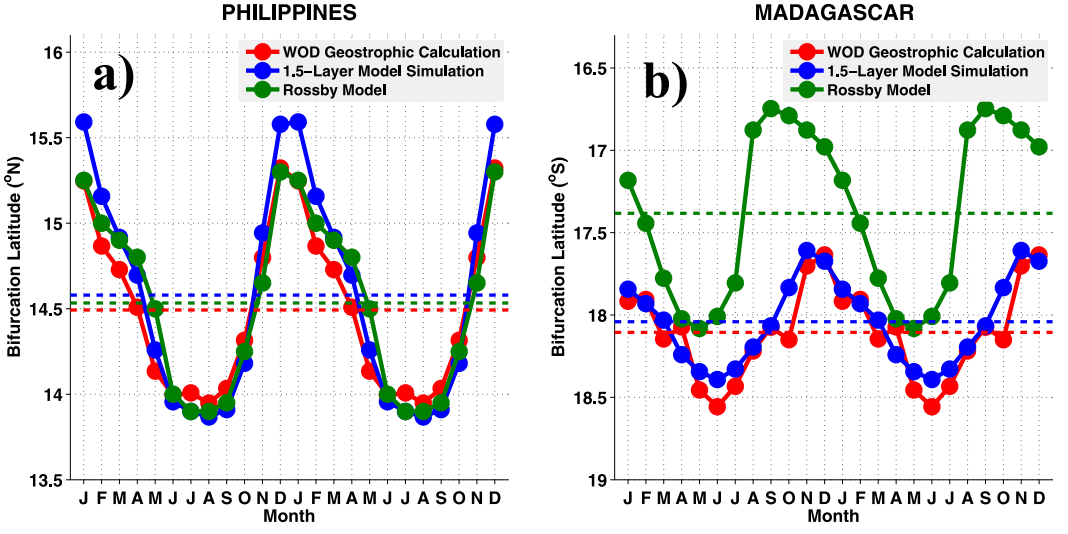

FIG. 5. Seasonal variation of the (a) NEC bifurcation off the Philippines coast and (b) SEC bifurcation off the Madagascar coast derived from the geostrophic calculation of *WOD09* (red), numerical simulation of a 1.5-layer nonlinear reduced gravity model (blue), and a Rossby model forced by wind stress curl (green). The dashed lines denote the mean values of respective seasonal cycles.

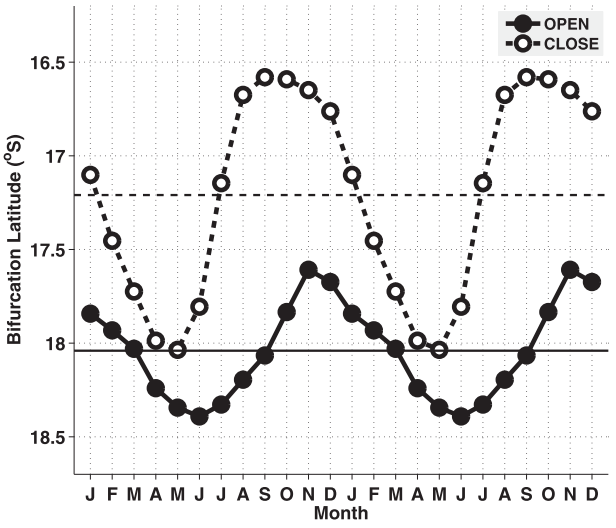

FIG. 6. Seasonal variation of the SBL derived from a 1.5-layer nonlinear reduced gravity model. The model simulations adopt a full Indian Ocean Basin geometry with (solid curve) and without (dashed curve) the Mozambique Channel. The straight lines denote the mean values of respective seasonal cycles.

of generating the seasonal cycle of the SBL despite that the barotropic response has been considered to be important in previous studies (e.g., Matano et al. 2002, 2008). Because the baroclinic processes are central to the upper-ocean processes in the SIO (Kindle 1991; Masumoto and Meyers 1998) and the goal of this study is to clarify the SEC bifurcation within the upper thermocline, we believe that the 1.5-layer model dynamics are relevant and sufficient in understanding the seasonal SBL variability. For the 1.5-layer model results presented in Fig. 5b, we have ignored the presence of the Indonesian Throughflow (ITF), which will be discussed in section 4. In comparison to that in the Pacific, the Rossby model fails to reproduce the seasonal cycle of the SEC bifurcation in the SIO. As shown in Fig. 5b, the mean SBL from the Rossby model is biased northward by more than 0.6° compared with the observations. In addition, the seasonal peaks are 1–2 months earlier than those in the 1.5-layer model.

The difference between the Rossby model and the 1.5-layer model implies that the cause is due to the neglect of either nonlinearity and/or topography in the Rossby model. Our additional numerical experiments confirm that it is the presence of the Madagascar Island that is responsible for this difference. Specifically, Fig. 6 shows that the seasonal SBL variation similar to that in the Rossby model is obtained in the experiment in which the Mozambique Channel is closed. To understand this result, we explore in the following subsection the relevant dynamics governing the SEC bifurcation off an isolated island, rather than a continent.

c. Role of an island in governing the mean position of the SEC bifurcation

Classical Sverdrup theory predicts that the bifurcation latitude of a zonal equatorial current coincides with the zero wind stress curl line (Pedlosky 1996). This, however, is no longer the case if the bifurcation occurs off the coast of an island. According to Godfrey's island rule (Godfrey 1989), the net transport T_0 between an island and the eastern boundary (EB) is commonly nonzero. In this case, the bifurcation, which is the same as the stagnation point proposed by Pedlosky et al. (1997), will be located at the latitude where the interior Sverdrup transport T_{in} is equal to T_0.

Assuming that the Indian Ocean is a semienclosed basin with no ITF entering into it, the net transport T_0 between Madagascar and the Australian continent is given by the Godfrey's island rule:

$$T_0 = -\frac{1}{\rho_0(f_{M_1} - f_{M_2})}\oint_{M_1A_1A_2M_2} \boldsymbol{\tau} d\mathbf{l}, \qquad (2)$$

where $M_1A_1A_2M_2$ is the contour delimited by the western flank of Madagascar, the EB, and the latitudes of the northern/southern tips of the island (see Fig. 7); f_{M_1} and f_{M_2} are the Coriolis parameters at the northern and southern latitudes, respectively; $\boldsymbol{\tau}$ is the wind stress and $d\mathbf{l}$ is the line segment along the integral path; and ρ_0 is the reference density of the seawater, taken to be 1025 kg m^{-3}. In terms of the steady-state circulation, the net transport T_0 between Madagascar and Australia using the ECMWF ORA-S3 wind stress data are about 5 Sverdrups (Sv; 1 Sv = 10^6 m^3 s^{-1}) northward. This leads to a southward shift of the bifurcation latitude by about 0.8°, or to 18.3°S, when compared to the zero wind stress curl line (the blue dot in Fig. 7).

d. A time-dependent island rule model

The above-mentioned island rule is valid only when the steady-state SBL off the Madagascar coast is considered. The realistic wind forcing in the SIO varies both in space and time and this motivates us next to examine the time-varying SEC bifurcation off the Madagascar coast by extending the island rule to its time-dependent form.

The study of Firing et al. (1999, hereafter F99) laid an important foundation for understanding the variability of a western boundary current east of an isolated island in a midocean. Here we follow the time-dependent island rule (TDIR) theory put forward by F99 and apply it to the time-varying SEC bifurcation off the Madagascar coast. Compared to F99, the governing dynamics in this study is simplified and will be that of the linear, 1.5-layer reduced gravity model:

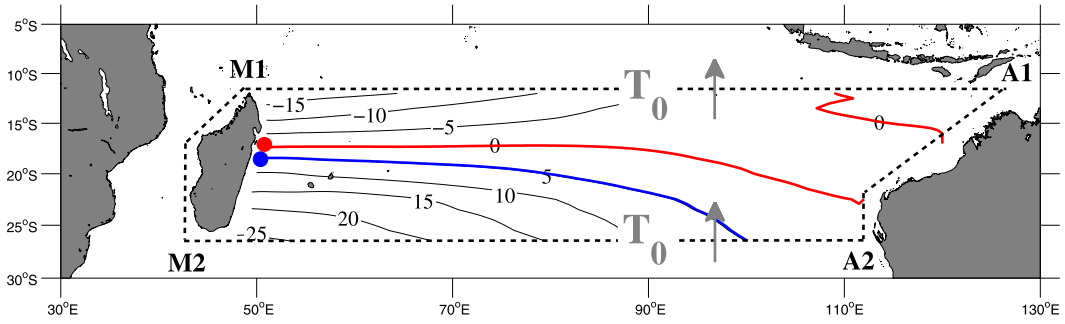

FIG. 7. Map of interior Sverdrup transport derived from the ECMWF ORA-S3 wind stress data. The red line denotes the zero contour of the Sverdrup transport and the blue line is the 5-Sv contour. The dashed line indicates the integral route of the island rule.

$$f\mathbf{k}\times\mathbf{u} = -g'\nabla h + \frac{\boldsymbol{\tau}}{\rho_0 H} + F(\mathbf{u}) \quad \text{and} \tag{3a}$$

$$\frac{\partial h}{\partial t} + H\nabla\cdot\mathbf{u} = 0, \tag{3b}$$

where $F(\mathbf{u})$ denotes the horizontal momentum dissipation due to interfacial friction or lateral eddy mixing, which is important only within the thin boundary layer east of the island; h is the time-varying upper-layer thickness; and H is the time-mean upper-layer thickness. Following F99, we neglect the $\partial\mathbf{u}/\partial t$ term in (3a) to adopt the long Rossby wave approximation and to make the Kelvin wave adjustments instantaneous around the island. We separate the ocean into a large interior region and an isolated midocean island region (Fig. 8). Notice that only the first baroclinic mode is considered. Taking the curl of (3a) and combining (3b) leads to the following equation for the interior region:

$$\frac{\partial h}{\partial t} + C_R\frac{\partial h}{\partial x} = -\nabla\times\left(\frac{\boldsymbol{\tau}}{\rho_0 f}\right) \equiv B(x,y,t), \tag{4}$$

where $C_R = -\beta g' H/f^2$ is the baroclinic long Rossby wave speed. By integrating (4) and neglecting the contribution from the EB forcing, we obtain

$$h(x,y,t) = \frac{1}{C_R}\int_{x_e}^{x} B\left(x', y, t - \frac{x-x'}{C_R}\right)dx'. \tag{5}$$

First, we calculate the total interior meridional transport across a fixed latitude y east of the island:

$$T_{\text{in}}(y,t) \equiv \int_{x_{w+}(y)}^{x_e(y)} Hv\,dx. \tag{6}$$

Using (5) and the linearized zonal momentum equation in (3a), $T_{\text{in}}(y, t)$ can be expressed by

$$T_{\text{in}}(y,t) = \int_{x_e}^{x_{w+}}\frac{\tau^x}{\rho_0 f}dx' - \frac{g'H}{fC_R}\int_{x_e}^{x_{w+}} B\left(x', y, t - \frac{x_{w+}-x'}{C_R}\right)dx'. \tag{7}$$

The first term in (7) denotes the meridional Ekman transport; the second term is the geostrophic transport associated with the baroclinic response to Ekman pumping.

Next, we consider the meridional transport within the boundary layer east of the island:

$$T_{\text{bc}}(y,t) \equiv \int_{x_w(y)}^{x_{w+}(y)} Hv\,dx. \tag{8}$$

Using the mass balance inside the boundary layer and ignoring the local divergence, we have

$$T_{\text{bc}}(y_n,t) - T_{\text{bc}}(y_s,t) + \int_{C_{w+}} H\mathbf{k}\times\mathbf{u}\cdot d\mathbf{l} = 0, \tag{9}$$

where C_{w+} is the segment of C_1 that runs along the offshore edge of the boundary current from the northern tip to the southern tip of the island (dashed line in

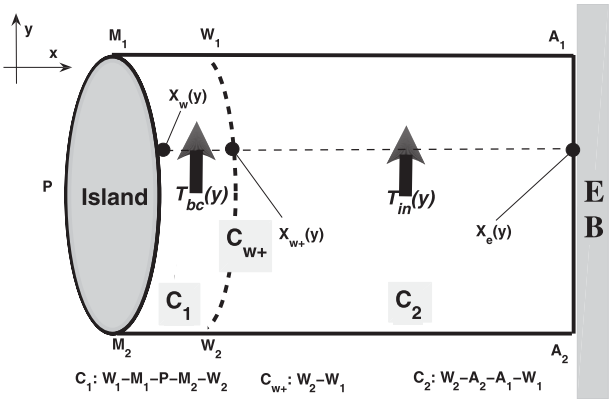

FIG. 8. Schematic defining integral paths for the time-dependent island rule: $M_1(y_n)$ and $M_2(y_s)$ are the northern and southern tips of the islands, $x_w(y)$ and $x_e(y)$ are the lon of the island's east coast and the ocean's eastern boundary at lat y, and $x_{w+}(y)$ is lon at the offshore edge (C_{w+}, the dashed line) of the island's western boundary layer. The term $T_{\text{bc}}(y)$ denotes the meridional transport of the western boundary current, and $T_{\text{in}}(y)$ is the interior meridional transport between $x_{w+}(y)$ and $x_e(y)$.

Fig. 8). To determine $T_{bc}(y_n, t)$, we follow Godfrey's island rule (Godfrey 1989)

$$\oint_{C_1} f\mathbf{k}\times\mathbf{u}\cdot d\mathbf{l} = \oint_{C_1}\frac{\boldsymbol{\tau}(t)\cdot d\mathbf{l}}{\rho_0 H}, \tag{10}$$

which implies that the vorticity input from the local wind is mainly balanced by the outward flux of planetary vorticity. Adopting the β-plane approximation $f = f_s + \beta(y - y_s)$, the above equation becomes

$$\beta\oint_{C_1} y\mathbf{k}\times\mathbf{u}\cdot d\mathbf{l} = \oint_{C_1}\frac{\boldsymbol{\tau}(t)\cdot d\mathbf{l}}{\rho_0 H} \tag{11}$$

or

$$y_n T_{bc}(y_n,t) - y_s T_{bc}(y_s,t) + \int_{C_{w+}} yH\mathbf{k}\times\mathbf{u}\cdot d\mathbf{l} = \oint_{C_1}\frac{\boldsymbol{\tau}(t)\cdot d\mathbf{l}}{\rho_0\beta}. \tag{12}$$

Eliminating $T_{bc}(y_s, t)$ from (9) and (12), we have

$$T_{bc}(y_n,t) = \frac{1}{\Delta y}\oint_{C_1}\frac{\boldsymbol{\tau}(t)\cdot d\mathbf{l}}{\rho_0\beta} - \frac{1}{\Delta y}\int_{C_{w+}}(y - y_s)H\mathbf{k}\times\mathbf{u}\cdot d\mathbf{l}, \tag{13}$$

where $\Delta y = y_n - y_s$. As is discussed in F99, this is the most physically meaningful expression for the boundary current transport. The first term on the rhs of (13) represents the response to local wind forcing around the island, and the second term on the rhs of (13) gives the western boundary response from the ocean interior. To evaluate the last term in (13), we use the linearized mass conservation (3b) and integrate it from x_{w+} to x_e with nonslip and no-normal flow conditions:

$$\begin{aligned}\int_{x_{w+}}^{x_e}\frac{\partial h}{\partial t}dx &= -H\int_{x_{w+}}^{x_e}\frac{\partial u}{\partial x}dx - H\int_{x_{w+}}^{x_e}\frac{\partial v}{\partial y}dx\\ &= Hu(x_{w+}) - \frac{\partial}{\partial y}T_{in}(y,t) - Hv(x_{w+})\frac{dx_{w+}}{dy}.\end{aligned} \tag{14}$$

The last term in (14) above comes from the following Leibniz rule:

$$\frac{\partial}{\partial y}\int_{x_{w+}}^{x_e} v\,dx = \int_{x_{w+}}^{x_e}\frac{\partial v}{\partial y}dx + v(x_e)\frac{dx_e}{dy} - v(x_{w+})\frac{dx_{w+}}{dy}. \tag{15}$$

Multiplying (14) by $(y - y_s)$, integrating in y, and substituting in (13), we have

$$\begin{aligned}T_{bc}(y_n,t) &= \frac{1}{\Delta y}\oint_{C_1}\frac{\boldsymbol{\tau}(t)\cdot d\mathbf{l}}{\rho_0\beta} - \frac{1}{\Delta y}\int_{y_s}^{y_n}\int_{x_{w+}}^{x_e}(y - y_s)\frac{\partial h}{\partial t}dx\,dy - \frac{1}{\Delta y}\int_{y_s}^{y_n}(y - y_s)\frac{\partial}{\partial y}T_{in}(y,t)\,dy\\ &= \frac{1}{\Delta y}\oint_{C_1}\frac{\boldsymbol{\tau}(t)\cdot d\mathbf{l}}{\rho_0\beta} - \frac{1}{\Delta y}\int_{y_s}^{y_n}\int_{x_{w+}}^{x_e}(y - y_s)\frac{\partial h}{\partial t}dx\,dy - T_{in}(y_n,t) + \frac{1}{\Delta y}\int_{y_s}^{y_n}T_{in}(y,t)\,dy.\end{aligned} \tag{16}$$

This provides the expression of the meridional transport within the western boundary at the northern tip off the island. The first rhs term is again the local wind forcing around the island. The second term, depending on the rate of change of averaged upper-layer thickness, can be called the ''storage'' term as suggested in F99, and vanishes in the low-frequency limit. The third and fourth terms are the meridionally averaged interior transport minus the local interior transport along y_n.

After obtaining the transport of the western boundary current at y_n, it is straightforward to derive the boundary current transport at any other latitude y by using the linearized mass conservation (3b) inside the box between y and y_n east of the island:

$$\begin{aligned}T_{bc}(y,t) &= T_{bc}(y_n,t) + T_{in}(y_n,t) - T_{in}(y,t)\\ &\quad + \int_y^{y_n}\int_{x_{w+}}^{x_e}\frac{\partial h}{\partial t}dx\,dy\end{aligned} \tag{17}$$

or

$$T_{bc}(y,t) = \begin{cases} -T_{in}(y,t)\\ +\dfrac{1}{\Delta y}\displaystyle\oint_{C_1}\frac{\boldsymbol{\tau}(t)\cdot d\mathbf{l}}{\rho_0\beta} + \frac{1}{\Delta y}\int_{y_s}^{y_n}T_{in}(y,t)\,dy\\ +\displaystyle\int_y^{y_n}\int_{x_{w+}}^{x_e}\frac{\partial h}{\partial t}dx\,dy - \frac{1}{\Delta y}\int_{y_s}^{y_n}\int_{x_{w+}}^{x_e}(y - y_s)\frac{\partial h}{\partial t}dx\,dy\end{cases}. \tag{18}$$

According to (18), the transport of the western boundary current east of an island is controlled by three terms: the response to the local interior transport in (18), top term; net transport between the island and the eastern boundary of the ocean basin in (18), middle term; and the storage that releases/stores the water in the ocean interior due to the seasonally varying upper-layer thickness (or thermocline depth) in (18), bottom term. Given the time-dependent surface wind stress forcing, $T_{bc}(y, t)$ in (18) can be evaluated numerically with the help of (5) and (7). By definition, the SEC bifurcation occurs at $y = Y_b$ where $T_{bc}(Y_b, t) = 0$.

Figure 9 shows the seasonal variation of the SBL derived from the 1.5-layer TDIR model. The result (the solid curve in Fig. 9) is in good agreement with both the observations and the 1.5-layer model simulation (Fig. 5b), with its southernmost position at 18.7°S in June and the northernmost position at 17.8°S in November. The mean position of the SBL, however, exhibits a southward shift of over 0.2° compared with the 1.5-layer model simulation and observational results (Fig. 5b). This discrepancy may result from the neglect of nonlinearity associated with the eddy shedding at the southern and northern tips of Madagascar as well as the frictional effects. Both the nonlinear and friction effects in the 1.5-layer model or in the real ocean would dissipate some of the vorticity input from the wind stress curl, leading to a smaller T_0 value than the island rule would predict (Yang et al. 2013). Overall, the time-dependent Godfrey's island rule is able to dynamically explain the mean position and seasonal variation of the SBL.

The dashed curve in Fig. 9 shows the SBL time series from the Rossby model, and differs from the TDIR model result both in terms of the seasonal peaks (by almost 1–2 months) and the mean position. This difference points to the role played by the island in modulating the seasonal cycle of the SEC bifurcation. To verify this, we evaluate the relative importance of each term in (18) that contributes to T_{bc} at 18.3°S (approximately near the mean Y_b derived from the TDIR). Consistent with the seasonal SBL variation, the western boundary transport at 18.3°S displays a distinct seasonal cycle with the peak seasons in June and November/December (Fig. 10a); that is, a positive (negative) anomaly in T_{bc} corresponds to a southward (northward) shift of the bifurcation. Further detailed examinations indicate that the seasonal evolution of T_{bc} at 18.3°S is predominantly determined by the (18) top and middle terms, while the (18) bottom term contributes little to its mean and seasonal variation (Fig. 10).

It is worth noting that the two terms in the (18) bottom term are perfectly balanced by each other, as shown in Fig. 10d. To better understand the contributions of the (18) bottom term to T_{bc} at each latitude, we further plot in Fig. 11 the time–latitude contour of the (18) bottom term. It is found that the storage is almost zero, or at least exhibits a very weak annual range near the bifurcation latitude of SEC either in the analytical/numerical model or in the ocean reanalysis. While far away from the bifurcation, the storage has more significant influence on T_{bc}. For instance, the storage strengthens the western boundary current off the Madagascar coast in the first half of the year, while it weakens it in the second half (Fig. 11).

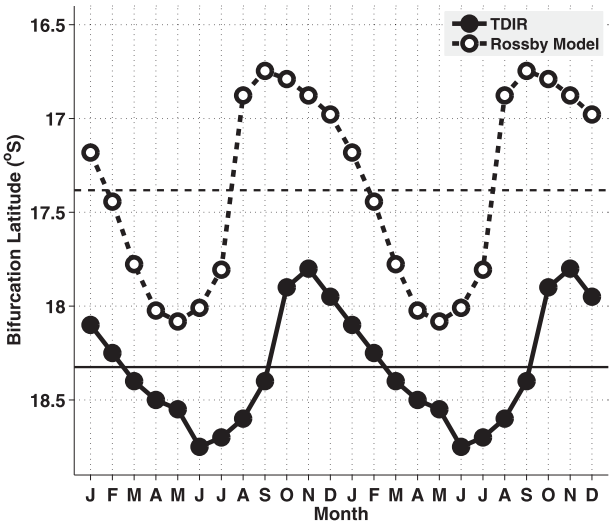

FIG. 9. Seasonal variation of the SBL derived from a Rossby model (dashed curve) and a linear, time-dependent island rule model (solid curve). The straight lines denote the mean values of respective seasonal cycles.

In the case of an island, there generally exists a nonzero total transport between the island and the eastern boundary according to the TDIR model (Fig. 10c). If Madagascar was connected to Africa, T_{bc} would be entirely balanced by the local interior transport. In this case, the mean SBL should move back to 17.4°S where the annual-mean local interior transport is zero (i.e., zero wind stress curl line) and the peak seasons of the SBL would shift accordingly, as the Rossby model results indicated (recall Fig. 9).

4. Summary and discussions

In this study, we investigated the seasonal variation of the South Equatorial Current bifurcation off the Madagascar coast in the upper south Indian Ocean based on an updated version of the *World Ocean Database 2009* and the 19-year satellite altimeter observations. The geostrophic calculation indicates that the SEC is largely

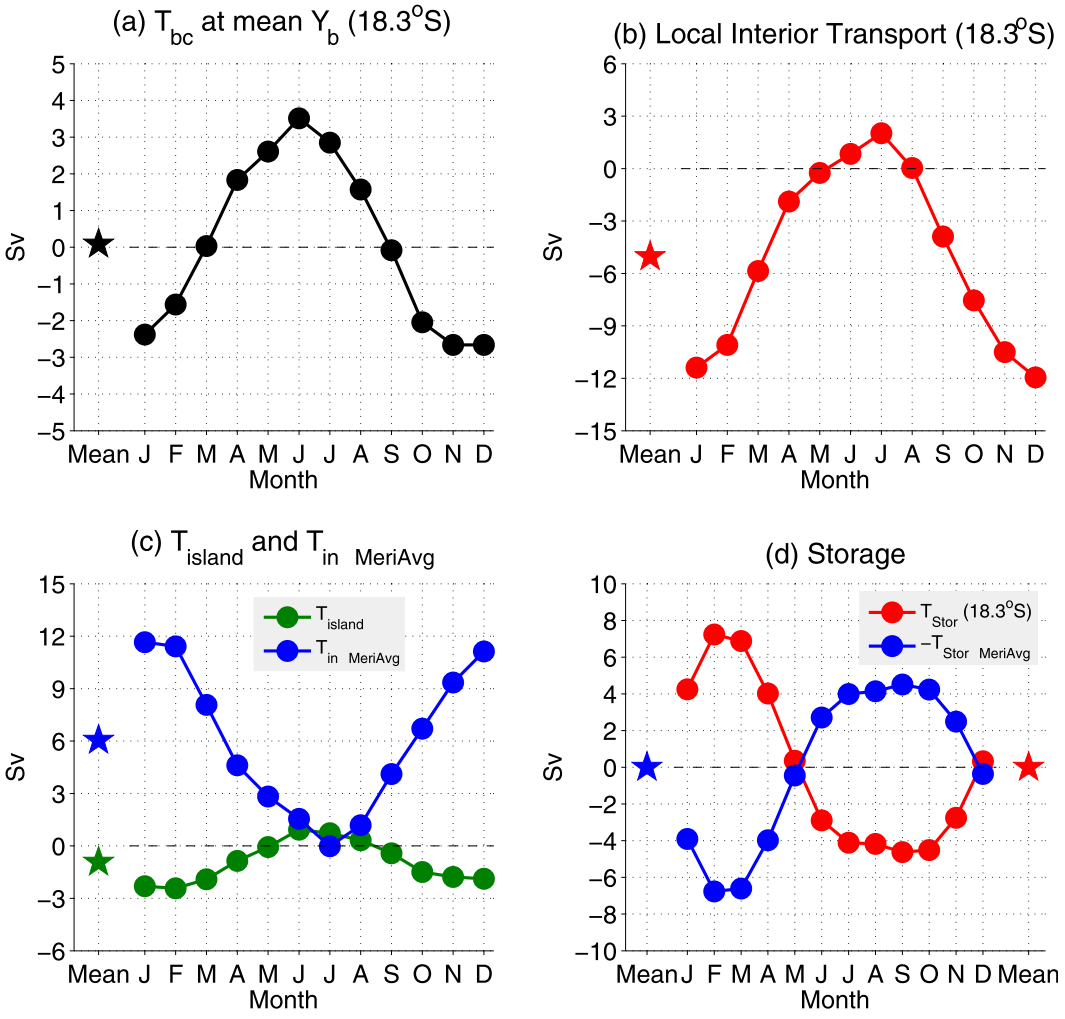

FIG. 10. Seasonal evolution of (a) western boundary current transport at mean bifurcation lat (18.3°S), (b) local interior transport at 18.3°S, (c) circumisland transport induced by the alongshore winds (green) vs meridionally averaged interior transport (blue), and (d) meridionally averaged storage (blue) vs local storage north of 18.3°S (red). The star denotes the mean value of respective seasonal cycles.

confined to the upper 400 m, with its bifurcation latitude exhibiting a poleward tilting with increasing depth. The SEC bifurcation shifts from 17.5°S at the surface to 19°S at 400 m, and its depth-integrated mean position occurs at 18.1°S.

With regard to its seasonal variation, the SEC bifurcation latitude moves to the southernmost position in June/July and the northernmost position in November/December. The large discrepancy between the annual excursion of the zero line of zonally integrated wind stress curl in the SIO (about 8°–9°) and that of the SBL (1°–1.5°) points to the importance of the baroclinic adjustment processes in controlling the seasonal variation of the SEC bifurcation within the upper thermocline. Contrary to the Pacific Ocean where both the 1.5-layer nonlinear reduced gravity model and the Rossby model are capable of reproducing the seasonal variation of the NEC bifurcation off the Philippine coast, the Rossby model fails to do so for the SEC bifurcation in the SIO (e.g., its seasonal phase and mean position). This implies that the Rossby wave dynamics alone are not sufficient to explain the seasonal variation of the SBL off the Madagascar coast. Like in the Pacific Ocean case, however, the 1.5-layer nonlinear reduced gravity model simulates well the SEC bifurcation.

Our detailed examinations revealed that the presence of Madagascar in the SIO makes the SEC bifurcation different from that of the NEC in the North Pacific. The zero wind stress curl line does not predict its mean position because the total transport between Madagascar and the Australian continent is nonzero and about 5 Sv northward. This sizable meridional transport alters the

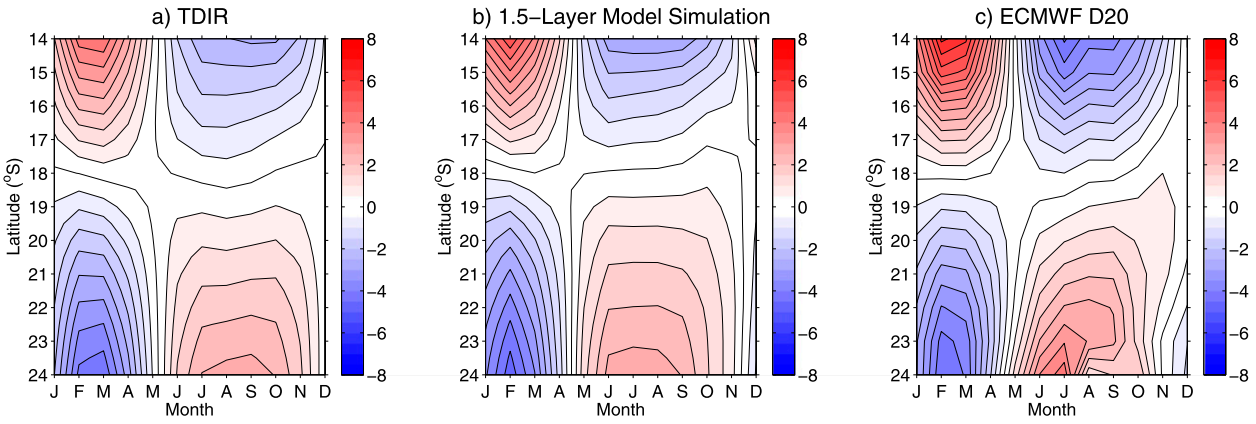

FIG. 11. Time–latitude plot of storage [(18), bottom term] (Sv). The values are derived from (a) TDIR, (b) 1.5-layer model, and (c) depth of 20°C data from ECMWF ORA-S3.

western boundary current off the Madagascar coast and shifts the SEC bifurcation latitude southward by about 0.8° relative to that predicted by the zero wind stress curl line. To understand the seasonal cycle of the SEC bifurcation, we adopted a linear time-dependent island rule (TDIR) model that combined the effect of island and the Rossby wave adjustment processes. The seasonal variation of the SBL derived from TDIR is consistent with the observations and the1.5-layer model simulation both in its mean position and peak seasons. Further examinations indicate that the presence of Madagascar works to moderately shift the SBL seasonal phase due to the additional effects of the circumisland transport and meridionally averaged interior transport.

Past observational and modeling studies have indicated that the existence of ITF allows for an input of Pacific water to cross the Indian Ocean and feed into the western boundary current system (e.g., Gordon 1986; Hirst and Godfrey 1993; Song et al. 2004; Valsala and Ikeda 2007; Zhou et al. 2008). It is speculated that the ITF would make a small contribution to the variation of SBL because it enters the Indian Ocean mostly north of Madagascar. So in our linear TDIR model and the 1.5-layer model, the ITF influence was not included. To quantify how the ITF affects the SEC bifurcation, we set up a double-basin run with a tunnel (regarded as ITF) connecting the Indian and Pacific Oceans. The ITF transport simulated from this double-basin model is shown in Fig. 12a; it has a mean transport of 9.1 Sv and a seasonal amplitude of 4.5 Sv. It is shown in Fig. 12b that compared with the non-ITF run, the mean SBL in the double-basin model is moved northward by 0.1°, and its seasonal peaks are shifted 1 month earlier. These model results indicate that the seasonal pulsing from the

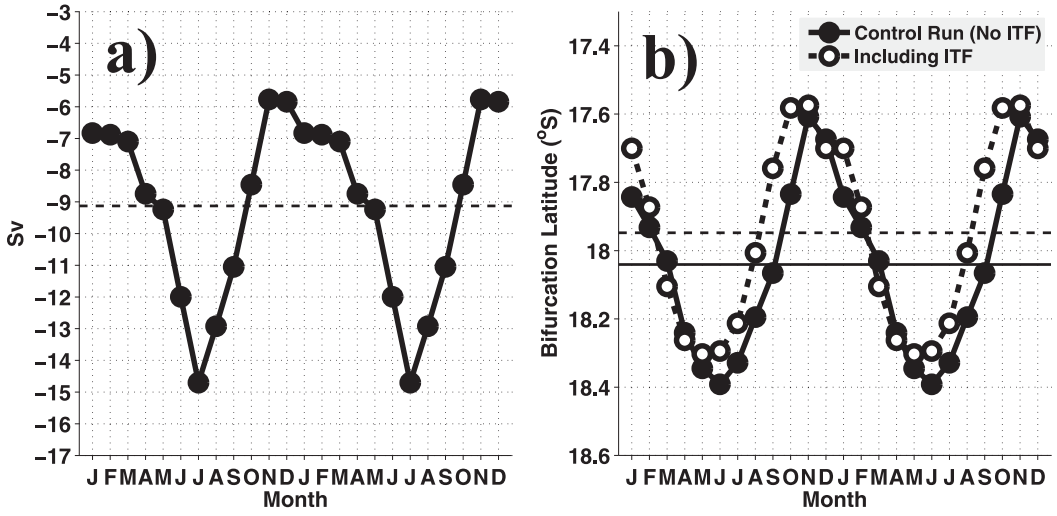

FIG. 12. (a) Seasonal variation of the ITF transport simulated in Indian–Pacific basin run. (b) Seasonal variation of the SBL derived from the control run (solid curve) and an Indian–Pacific basin run including ITF (dashed curve).

ITF does not induce a significant SBL change on the seasonal time scale. Physically, this is because only a small portion of the ITF water reaches the east coast of Madagascar (0.6 Sv); most of the ITF inflow passes through the Mozambique Channel (8.5 Sv) in the double-basin model run.

Our present work has mainly focused on the seasonal variation of the SEC bifurcation and, as discussed above, the Rossby wave dynamics are shown to play a predominant role. We expect that on longer time scales, the basinwide wind forcing and the non-wind-driven processes (e.g., the thermohaline forcing and the ITF injection) are likely to play a more significant role in determining the SBL as the baroclinic adjustment effects would average out. It will be important for future studies to explore the interannual-to-decadal changes of the mass and heat redistributions associated with the SEC bifurcation, as well as the expected variability under the global warming scenario.

Acknowledgments. We are indebted to the CLS Space Oceanography Division for providing us the merged satellite altimeter data. We thank Yukio Masumoto and another anonymous reviewer as well as editor Dr. William Kessler for their constructive comments, which improved the early version of the manuscript. Discussions with Dr. Zuowei Zhang and Dr. Xiaopei Lin are gratefully appreciated. This research is supported by National Science Foundation of China (41306001 and 41221063) and National Basic Research Program of China (2013CB956200).

APPENDIX

The 1.5-layer Nonlinear Reduced Gravity Model and the Rossby Model

The governing equations of the 1.5-layer nonlinear reduced gravity model are

$$\frac{\partial u}{\partial t}+u\frac{\partial u}{\partial x}+v\frac{\partial u}{\partial y}-fv+g'\frac{\partial h}{\partial x}=A_H\nabla^2 u+\frac{\tau^x}{\rho h}, \tag{A1}$$

$$\frac{\partial v}{\partial t}+u\frac{\partial v}{\partial x}+v\frac{\partial v}{\partial y}+fu+g'\frac{\partial h}{\partial y}=A_H\nabla^2 v+\frac{\tau^y}{\rho h}, \quad \text{and} \tag{A2}$$

$$\frac{\partial h}{\partial t}+\frac{\partial hu}{\partial x}+\frac{\partial hv}{\partial y}=0, \tag{A3}$$

where u and v are the zonal and meridional velocities, h is the upper-layer thickness, f is the Coriolis parameter, g' is the reduced gravity acceleration, A_H is the coefficient of horizontal eddy viscosity (set to be $500\,\mathrm{m^2\,s^{-1}}$), ρ is the reference water density, and τ^x and τ^y are the surface wind stresses. The initial upper-layer thickness is $H = 270$ m, which is equivalent to the mean depth of 26.6 σ_θ in the Indian Ocean derived from *World Ocean Atlas 2009* (*WOA09*) (Antonov et al. 2010; Locarnini et al. 2010). The density contrast between the abyssal ocean ($\rho = 1025\,\mathrm{kg\,m^{-3}}$) and the upper-layer ocean $\Delta\rho$ is $3\,\mathrm{kg\,m^{-3}}$; so, g' in the model is $0.029\,\mathrm{m\,s^{-2}}$.

The model domain covers the subtropical and tropical regions in the SIO, which extends from 45°S to 30°N in the meridional direction and from 30° to 130°E in the zonal direction. The horizontal resolution of the model is 0.5°, and marginal seas shallower than 200 m are treated as land. No-normal flow and nonslip boundary conditions are used along the coasts, and a free-slip condition is applied to the southern open boundary at 45°S. It should be mentioned that A_H in the model increases linearly from $500\,\mathrm{m^2\,s^{-1}}$ at 25°S to $2000\,\mathrm{m^2\,s^{-1}}$ at 45°S for the purpose of suppressing instabilities and damping spurious coastal Kelvin waves along the artificial southern boundary. The model is first spun up by the mean wind stress derived from ECMWF ORA-S3 for 20 years until a statistical steady state is reached. After spinup, the model is forced by the seasonally varying wind stresses (monthly climatology) for an additional 20 years and this model run is denoted as the control run. For the Indian–Pacific basin model run, the model domain is extended eastward to 70°W. An artificial tunnel is introduced in this model run to allow for the inflow from the Indonesian archipelago, and an open channel is introduced for the outflow south of Australia. Outputs from the last 10 model years are used to construct the seasonal cycle of the SBL.

The Rossby model is derived from the primitive equation, which governs the 1.5-layer ocean by adopting the long wave approximation. The equation can be written as

$$\frac{\partial h}{\partial t}+C_R\frac{\partial h}{\partial x}=-\frac{1}{\rho_0}\nabla\times\frac{\boldsymbol{\tau}}{f}-\varepsilon h, \tag{A4}$$

where C_R is the phase speed of first-mode baroclinic long Rossby waves, h is the height deviation from the mean upper-layer thickness, f is the Coriolis parameter, ρ_0 is the mean density of the upper-layer ocean, and ε is the Newtonian dissipation rate with the unit of per year. In this study, we choose $\varepsilon = 0$. Other tests in which $\varepsilon^{-1} = 2$ and 5 yr are also used and it does not change the seasonal cycle of the SBL essentially (figures not shown). Integrating (A4) along the long Rossby wave characteristic line, we obtain

$$h(x,y,t)=\frac{1}{\rho_0}\int_{x_e}^{x}\frac{1}{C_R}\nabla\times\frac{\boldsymbol{\tau}}{f}\left(x',y,t-\frac{x-x'}{C_R}\right)dx'. \tag{A5}$$

In (A5), we have ignored that part of the solution due to the EB forcing because its influence is limited to the EB (e.g., Fu and Qiu 2002; Cabanes et al. 2006). Following Qiu and Lukas (1996), mass conservation requires the inflow at the western boundary to bifurcate where $h = 0$ if the detailed flow structures inside the western boundary are neglected, so we define the SBL in the linear model at the position where mean h within 2° off the western boundary is zero.

REFERENCES

Antonov, J. I., and Coauthors, 2010: *Salinity.* Vol. 2, *World Ocean Atlas 2009,* NOAA Atlas NESDIS 69, 184 pp.

Balmaseda, M. A., A. Vidard, and D. L. T. Anderson, 2008: The ECMWF Ocean Analysis System: ORA-S3. *Mon. Wea. Rev.,* **136,** 3018–3034.

——, K. Mogensen, and A. T. Weaver, 2012: Evaluation of the ECMWF ocean reanalysis system ORAS4. *Quart. J. Roy. Meteor. Soc.,* **139,** 1132–1161, doi:10.1002/qj.2063.

Boyer, T. P., and Coauthors, 2009: *World Ocean Database 2009.* NOAA Atlas NESDIS 66, 216 pp.

Cabanes, C., T. Huck, and A. C. D. Verdière, 2006: Contributions of wind forcing and surface heating to interannual sea level variation in the Atlantic Ocean. *J. Phys. Oceanogr.,* **36,** 1739–1750.

Chapman, P., S. F. Di Marco, R. E. Davis, and A. C. Coward, 2003: Flow at intermediate depths around Madagascar based on ALACE float trajectories. *Deep-Sea Res.,* **50,** 1957–1986.

Chen, Z., and L. Wu, 2011: Dynamics of the seasonal variation of the North Equatorial Current bifurcation. *J. Geophys. Res.,* **116,** C02018, doi:10.1029/2010JC006664.

——, and ——, 2012: Long-term change of the Pacific North Equatorial Current bifurcation in SODA. *J. Geophys. Res.,* **117,** C06016, doi:10.1029/2011JC007814.

Donohue, K. A., and J. M. Toole, 2003: A near-synoptic survey of the southwest Indian Ocean. *Deep-Sea Res.,* **50,** 1893–1931.

Firing, E., B. Qiu, and W. Miao, 1999: Time-dependent island rule and its application to the time-varying North Hawaiian Ridge Current. *J. Phys. Oceanogr.,* **29,** 2671–2688.

Fu, L.-L., and B. Qiu, 2002: Low-frequency variability of the North Pacific Ocean: The roles of boundary- and wind-driven baroclinic Rossby waves. *J. Geophys. Res.,* **107,** 3220, doi:10.1029/2001JC001131.

Godfrey, J. S., 1989: A Sverdrup model of the depth-integrated flow for the World Ocean allowing for island circulations. *Geophys. Astrophys. Fluid Dyn.,* **45,** 89–112.

Gordon, A. L., 1986: Interocean exchange of thermocline water. *J. Geophys. Res.,* **91** (C4), 5037–5046.

Hastenrath, S., and L. Greischar, 1991: The monsoonal current regimes of the tropical Indian Ocean: Observed surface flow fields and their geostrophic and wind-driven components. *J. Geophys. Res.,* **96** (C7), 12 619–12 633.

Hirst, A. C., and J. S. Godfrey, 1993: The role of Indonesian Throughflow in a global ocean GCM. *J. Phys. Oceanogr.,* **23,** 1057–1086.

Jensen, T. G., 2011: Bifurcation of the Pacific North Equatorial Current in a wind-driven model: Response to climatological winds. *Ocean Dyn.,* **61,** 1329–1344, doi:10.1007/s10236-011-0427-2.

Jia, F., L. Wu, and B. Qiu, 2011: Seasonal modulation of eddy kinetic energy and its formation mechanism in the southeast Indian Ocean. *J. Phys. Oceanogr.,* **41,** 657–665.

Kim, Y. Y., T. Qu, T. Jensen, T. Miyama, H. Mitsudera, H.-W. Kang, and A. Ishida, 2004: Seasonal and interannual variation of the North Equatorial Current bifurcation in a high-resolution OGCM. *J. Geophys. Res.,* **109,** C03040, doi:10.1029/2003JC002013.

Kindle, J. C., 1991: Topographic effects on the seasonal circulation of the Indian Ocean. *J. Geophys. Res.,* **96** (C9), 16 827–16 837.

Locarnini, R. A., A. V. Mishonov, J. I. Antonov, T. P. Boyer, and H. E. Garcia, 2010: *Temperature.* Vol. 1, *World Ocean Atlas 2009,* NOAA Atlas NESDIS 68, 184 pp.

Lutjeharms, J. R. E., N. D. Bang, and C. P. Duncan, 1981: Characteristics of the current east and south of Madagascar. *Deep-Sea Res.,* **28,** 879–901.

Masumoto, Y., and G. Meyers, 1998: Forced Rossby waves in the southern tropical Indian Ocean. *J. Geophys. Res.,* **103** (C12), 27 589–27 602.

Matano, R. P., E. J. Beier, P. T. Strub, and R. Tokmakian, 2002: Large-scale forcing of the Agulhas variability: The seasonal cycle. *J. Phys. Oceanogr.,* **32,** 1228–1241.

——, ——, and ——, 2008: The seasonal variability of the circulation in the South Indian Ocean: Model and observations. *J. Mar. Syst.,* **74,** 315–328, doi:10.1016/j.jmarsys.2008.01.007.

Nauw, J. J., H. M. van Aken, A. Webb, J. R. E. Lutjeharms, and W. P. M. de Ruijter, 2008: Observations of the southern East Madagascar Current and Undercurrent and Countercurrent system. *J. Geophys. Res.,* **113,** C08006, doi:10.1029/2007JC004639.

Palastanga, V., P. J. van Leeuwen, and W. P. M. de Ruijter, 2006: A link between low-frequency mesoscale eddy variability around Madagascar and the large-scale Indian Ocean variability. *J. Geophys. Res.,* **111,** C09029, doi:10.1029/2005JC003081.

——, ——, M. W. Schouten, and W. P. M. de Ruijter, 2007: Flow structure and variability in the subtropical Indian Ocean: Instability of the South Indian Ocean Countercurrent. *J. Geophys. Res.,* **112,** C01001, doi:10.1029/2005JC003395.

Pedlosky, J., 1996: *Ocean Circulation Theory.* Springer-Verlag, 453 pp.

——, L. Pratt, M. Spall, and K. Helfrich, 1997: Circulation around islands and ridges. *J. Mar. Res.,* **55,** 1199–1251.

Qiu, B., and R. Lukas, 1996: Seasonal and interannual variability of the North Equatorial Current, the Mindanao Current, and the Kuroshio along the Pacific western boundary. *J. Geophys. Res.,* **101** (C5), 12 315–12 330.

——, and S. Chen, 2010: Interannual-to-decadal variability in the bifurcation of the North Equatorial Current off the Philippines. *J. Phys. Oceanogr.,* **40,** 2525–2538.

——, D. L. Rudnick, S. Chen, and Y. Kashino, 2013: Quasi-stationary North Equatorial Undercurrent jets across the tropical North Pacific Ocean. *Geophys. Res. Lett.,* **40,** 2183–2187, doi:10.1002/grl.50394.

Qu, T., and E. J. Lindstrom, 2002: A climatological interpretation of the circulation in the western South Pacific. *J. Phys. Oceanogr.,* **32,** 2492–2508.

——, and R. Lukas, 2003: The bifurcation of the North Equatorial Current in the Pacific. *J. Phys. Oceanogr.,* **33,** 5–18.

Ridderinkhof, H., P. M. van der Werf, J. E. Ullgren, H. M. van Aken, P. J. van Leeuwen, and W. P. M. de Ruijter, 2010: Seasonal and interannual variability in the Mozambique Channel from moored current observations. *J. Geophys. Res.,* **115,** C06010, doi:10.1029/2009JC005619.

Rio, M. H., S. Guinehut, and G. Larnicol, 2011: New CNES-CLS09 global mean dynamic topography computed from the combination of GRACE data, altimetry, and in situ

measurements. *J. Geophys. Res.,* **116,** C07018, doi:10.1029/2010JC006505.

Rodrigues, R. R., L. M. Rothstein, and M. Wimbush, 2007: Seasonal variability of the South Equatorial Current bifurcation in the Atlantic Ocean: A numerical study. *J. Phys. Oceanogr.,* **37,** 16–30.

Schott, F., and J. McCreary, 2001: The monsoon circulation of the Indian Ocean. *Prog. Oceanogr.,* **51,** 1–123.

——, M. Fieux, J. Kindle, J. Swallow, and R. Zantopp, 1988: The boundary currents east and north of Madagascar: 2. Direct measurements and model comparisons. *J. Geophys. Res.,* **93** (C5), 4963–4974.

Siedler, G., M. Rouault, and J. R. E. Lutjeharms, 2006: Structure and origin of the subtropical South Indian Ocean Countercurrent. *Geophys. Res. Lett.,* **33,** L24609, doi:10.1029/2006GL027399.

——, ——, A. Biastoch, B. Backeberg, C. J. C. Reason, and J. R. E. Lutjeharms, 2009: Modes of the southern extension of the East Madagascar Current. *J. Geophys. Res.,* **114,** C01005, doi:10.1029/2008JC004921.

Song, Q., A. Gordon, and M. Visbeck, 2004: Spreading of the Indonesian Throughflow in the Indian Ocean. *J. Phys. Oceanogr.,* **34,** 772–792.

Stramma, L., and J. R. E. Lutjeharms, 1997: The flow field of the subtropical gyre of the South Indian Ocean. *J. Geophys. Res.,* **102** (C3), 5513–5530.

Swallow, J., M. Fieux, and F. Schott, 1988: The boundary currents east and north of Madagascar: 1. Geostrophic currents and transports. *J. Geophys. Res.,* **93** (C5), 4951–4962.

Toole, J. M., R. C. Millard, Z. Wang, and S. Pu, 1990: Observations of the Pacific North Equatorial Current bifurcation at the Philippine coast. *J. Phys. Oceanogr.,* **20,** 307–318.

Valsala, V. K., and M. Ikeda, 2007: Pathways and effects of the Indonesian Throughflow water in the Indian Ocean using particle trajectory and tracers in an OGCM. *J. Climate,* **20,** 2994–3017.

Wang, Q., and D. Hu, 2006: Bifurcation of the North Equatorial Current derived from altimetry in the Pacific Ocean. *J. Hydrodyn.,* **18,** 620–626, doi:10.1016/S1001-6058(06)60144-3.

Yang, J., X. Lin, and D. Wu, 2013: Wind-driven exchanges between two basins: Some topographic and latitudinal effects. *J. Geophys. Res. Oceans,* **118,** 4585–4599, doi:10.1002/jgrc.20333.

Zhou, L., R. Murtugudde, and M. Jochum, 2008: Seasonal influence of Indonesian Throughflow in the southwestern Indian Ocean. *J. Phys. Oceanogr.,* **38,** 1529–1541.